AN ORBITAL LIGHT CURVE MODEL AND SPECTRAL FEATURES IN GX301-2

Steven H. Pravdo[1,2,3]
and
Lorella Angelini[3,4]

and

Pranab Ghosh[5, 6]

submitted to the *Astrophysical Journal*, 15 October 1999

---

[1]The research described in this paper was carried out in part by the Jet Propulsion Laboratory, California Institute of Technology, under contract with the National Aeronautics and Space Administration.

[2]Jet Propulsion Laboratory, Mail Stop 306-431, California Institute of Technology, Pasadena, CA 91109. email: spravdo@ccmail.jpl.nasa.gov

[3]*ASCA* and *RXTE* guest investigator

[4]University Space Research Association, Laboratory for High Energy Astrophysics, NASA/Goddard Space Flight Center, Code 668, Greenbelt, MD 20771. email: day@lheavx.gsfc.nasa.gov and angelini@lheavx.gsfc.nasa.gov

[5]Senior NAS/NRC Fellow

[6] Code 662, Laboratory for High Energy Astrophysics, NASA Goddard Space Flight Center, Greenbelt, MD 20771

ABSTRACT

We present the results of X-ray observations of GX301-2 with instruments aboard the *ASCA* and *RXTE* spacecraft, as well as analysis of archival data from BATSE/*CGRO* and the All-Sky Monitor on *RXTE*. We discuss evidence that (1) GX301-2 has changed its spin state, perhaps entering a stochastic spin state similar to1974-1984; (2) epochal changes occur in the constant and flaring components of the orbital light curve – a 25% increase in the overall luminosity is coincident with the changed spin state and is due to an increase in the constant component accompanied by a decrease in the near-apastron flare, (3) the orbital light curve, in general, and timing of the pre-periastron flare, in particular, can be understood as a latency effect in the GX301-2 accretion disk; (4) Kβ emission is detected; and (5) GX301-2 exhibits cyclotron features that imply a surface magnetic field value of 9×10^{11} G.

Subject headings: stars: individual (GX301-2)--X-rays: stars

1. INTRODUCTION

GX301-2 is an X-ray pulsar in a binary system with the supergiant WRA 977 (B1.5 Ia). Many of its interesting X-ray properties arise from its 41.498-day orbital period and high eccentricity, ε = 0.422 (Sato et al. 1986, Koh et al. 1997). The neutron star is a strong X-ray source, $L_x \sim 10^{37}$ ergs s^{-1}, due to significant mass accretion from its companion. A strong X-ray flare occurs before most periastron passages with an intensity profile that is asymmetric in phase with respect to periastron. Variations in the WRA 977 stellar wind can not account for the X-ray intensity variations with orbital phase (e.g. White and Swank 1984), nor can tidal mass transfer (e.g. Layton et al. 1998). Various models, mostly phenomenological, have attempted to account for this behavior (e.g. Haberl 1991 and Leahy 1991 following Stevens 1988; Chichkov 1995). Pravdo et al. (1995; hereafter P95) discovered a periodic near-apastron (NA) flare with lower intensity than the pre-periastron (PP) flare which they attributed to enhanced accretion from material in a circumstellar disk around WRA 977 (see also Koh et al 1997).

The source was identified as a pulsar by White et al. (1976). Between 1973 and 1984 the pulse period behavior with time was stochastic (Nagase 1989) leading to an explanation based upon angular momentum transferred via a stellar wind (e.g. White & Swank 1984). Since 1984 a secular spin-up has occurred which, according to the theory of Ghosh & Lamb (1979), indicates that an accretion disk has formed.

The X-ray continuum spectrum is typical of many binary X-ray pulsars and consists of a power-law with a high-energy cutoff (e.g. White, Swank, & Holt 1983). In addition, GX301-2 has episodes of enhanced low-energy absorption (Ricker *et al.* 1973), an iron absorption edge (Swank et al. 1976), pulse-phase dependence (Leahy & Matsuoka 1990), orbital-phase dependence (Haberl 1991), iron Kα-line emission (Leahy et al.1989), and low-energy lines (Saraswat et al. 1996).

This paper reports the results of six observations of GX301-2 , three obtained with *ASCA* and three with *Rossi X-ray Timing Explorer (RXTE)*. The earliest *ASCA* observation has already been discussed by P95 and Saraswat et al. (1996). In addition, we make use of the public archives of *RXTE* All-Sky Monitor (ASM) and *Compton Gamma-Ray Observatory* (*CGRO*) Burst and Transient Source Experiment (BATSE) data to examine the longer term history of the source.

2. OBSERVATIONS

Table 1 lists the six observations of GX301-2 that are discussed herein. *ASCA* observed GX301-2 on 13-14 February 1994 (*AQ*), 26-27 January 1996 (*AA*), and 16-17 February 1996 (*AP*). The *ASCA* telescope and detectors are described by Tanaka et al. (1994). We use both Solid-state Imaging Spectrometer (SIS) and Gas Imaging Spectrometer (GIS) data in the 0.3-10 keV range: the SIS for its superior energy resolution (about a factor of 4 compared to the GIS) and the GIS for its enhanced high-energy response (E > 5 keV).

The Rossi X-ray Timing Exploring (*RXTE*) observed GX301-2 on 12-3 September (*XP*), 12-3 November (*XA*), and 23-4 November 1996 (*XQ*). Data were obtained from two sets of detectors: (1) the Proportional Counter Array (PCA) consisting of 5 proportional counters and (2) the High-Energy X-ray Timing Experiment (HEXTE) consisting of 2 clusters of four NaI(Tl)/CsI(Na) phoswich scintillation counters. All the PCA detectors were operating, except during the 23-4 November1996 observations when 2 detectors intermittently turned off, as were the 8 HEXTE

counters, although one of the latter did not provide spectral information. The PCA and HEXTE energy ranges were 3-60, and 16-250 keV, respectively. Observing times of the PCA and HEXTE detectors substantially overlapped but were not identical since the detectors have different operational modes. In particular, HEXTE rocks between on- and off-source positions leading to a reduction of on-source time by >50%.

The publicly archived *RXTE* All-Sky Monitor (ASM) and BATSE */CGRO* data provide nearly continuous coverage of GX301-2 except for periods of Earth occultation of the source or detector shutdown (e.g. during passages of the South Atlantic Anomaly). The ASM consists of three position-sensitive proportional counters sensitive in the 2-12 keV range that view the sky through a slit mask to infer the directions and intensities of the sources (Levine et al. 1996). BATSE consists of eight uncollimated NaI scintillation crystal detectors BATSE (Fishman et al. 1989) that provide intensity data in the energy range 20-50 keV after Earth-occultation analysis (e.g. Prince et al. 1994).

3. RESULTS

3.1 X-RAY TIMING RESULTS

3.1.1 Pulse Periods

Table 1 also lists the pulse periods results. Periods are determined by folding the barycentric- and GX 301-binary period-corrected timing data over trial pulse periods. Data are from the *ASCA*/GIS and the *RXTE*/PCA detectors. The intrinsic time resolutions are 0.5 s and 16 s, respectively. χ^2 is calculated for a range of periods and the best period chosen from the peak of a Gaussian function fit to the χ^2 vs. period curve. The uncertainties are the estimated three-sigma errors determined as discussed below. The last column shows the difference between periods determined contemporaneously with BATSE./*CGRO* (Koh 1995, Finger 1998). For BATSE the periods are determined with data that span from 3-11 days.

Because of the sometimes large differences shown in last column of Table 1 we examined carefully the pulse shapes and phases histories of our data. As a concrete example, we show the results for the *XP* data set, the one that has the largest difference, 0.35 s. The data are divided into 9 sub-intervals, each of which spans about 8 ks and contains about 10 pulses. Each sub-interval is folded over the best-fit period determined for the entire interval. Then the pulses from each sub-interval are compared with the template pulse from the entire interval to measure phase lags. Phase lags are plotted in Figure 1. There are two things to notice about the figure. First, the phase lag curves track each other well for different periods – the same bumps and wiggles persist. Second, the periods determined with PCA and BATSE have the closest to 0 (or equivalently, 1) average phase lag, as shown in the figure insert. The PCA average is the closest to 0 – this is why the fitting program chose the period. Other periods shown in the figure for comparison have average phase lags that increase both positively and negatively from 0.

Two of the pulses that comprise the sub-intervals and the template pulse from the *XP* data are shown in Figure 2. The pulses are shown in 50 phase bins, oversampled for the 16s- rate data. Errors due to counting statistics in each phase bin are comparable with the size of the symbols. Note the range of pulse shapes illustrated by sub-interval 6, wherein the secondary pulse maximum almost

disappears and, sub-interval 7, wherein the secondary pulse intensity nearly equals that of the primary pulse.

These pulse shape changes contribute to the phase-lags-jitter shown in Figure 1. The effects of pulse shape, phase, and period jitter are coupled. Period errors listed in Table 1 are estimated as three standard deviations of the phase lags measured for sub-intervals compared with templates from each data interval, as illustrated for *XP* data, above. Even so, these errors do not account for differences between the periods determined herein and those from BATSE – in 3 of 6 cases the differences are larger than 3 standard deviations.

The period differences may be due to the differing time spans over which the periods are determined -- about 1 day for the GIS and PCA, and 11 days for BATSE, except for the *AQ* data set. For that 3 days of BATSE data were employed, and indeed in that case the period measurements are within ~2σ. The BATSE periods are necessarily averaged over their longer time spans. The fact that the differences are largest for the periastron phases is discussed below.

Figure 3 shows the GX301-2 long-term period behavior. Our results are superimposed with historical data including the BATSE periods found in the online archive. It is believed that GX301-2 was secularly spinning up starting about JD 2446000. However, since about JD 2449000 this trend is not apparent.

3.1.2 Long-Term X-ray Behavior

We use the BATSE (http://cossc.gsfc.nasa.gov/cossc/batse/hilev/occ.html). and ASM (http://starchild.gsfc.nasa.gov/docs/xte/SOF/asmlc.html) data archives to examine the long-term X-ray behavior, searching in particular for correlations between the X-ray intensity and the period changes described above. Figure 4 shows the light curve of the BATSE data for about 2000 days. Each point consists of 3 orbital periods of data (or 124.5 days). To mitigate against the effects of any drift in detector performance these data are divided by contemporaneously obtained BATSE intensity data from the Crab, normalized to the average Crab intensity. To the extent that the Crab is a steady source and that any detector changes are source independent, then the GX 301-2 in the figure should be free of systematic detector effects.

It appears that the average 20-50 keV GX 301-2 intensity began to rise around MJD 49500. Interestingly, this is about the same time that the secular spin-up trend appears to have reversed, or at least paused. The average intensity after MJD 49500 is 0.052 ± 0.001 cts s^{-1} while that before this time is 0.040 ± 0.001 cts s^{-1}, or an increase of about 25%.

Is this intensity increase evenly distributed over orbital phase or do some orbital phases contribute more than others? Figure 5 shows the light curves folded over the GX 301-2 orbital period (BATSE + Sato epoch from Koh et al. 1997) for four sets of data: *(a)* all available data from the interval before that reported in P95, *(b)* the P95 interval, *(c)* after P95 but before MJD 50150.5 when the spin-up apparently ended, and *(d)* after MJD 50150.5. We analyzed these data by fitting the light curves with a model consisting of a constant and up to 3 Lorentzian functions, one each for the rising and falling portions of the PP flare and one for the NA flare. Note that the effective time resolution of these data do not allow the characterization of features with timescales of < 1 day. The PP flare was marginally asymmetric as reported in P95, when the rise was slower than the fall. But in all the other date intervals analyzed herein, any small asymmetry is in the opposite sense, with the fall slower

than the rise. For simplicity in Figure 6 we model the PP as a single Lorentzian. This figure shows that the total intensity in the PP flare varies by no more than 20% and the variation is not monotonic. The constant (or non-flaring) component increases over the last two data intervals by about a factor of 2, while the NA flare becomes vanishingly small. The increase in the constant components accounts for the overall increase in the GX301-2 intensity.

3.2 X-RAY SPECTRA

We use the archived data from the monitoring observations to demonstrate a general principal of the pulse-phase-averaged spectrum. Figure 7 shows contemporaneous ASM and BATSE data folded over the orbital period in the top and middle panels, respectively. The lower panel shows the ratio of the BATSE to the ASM intensities, a hardness measure since the ASM measures significantly lower energies, with a median energy at about 6 keV compared with > 20 keV for BATSE . The hardest spectrum occurs near orbital phase 0.2, a heretofore unobserved and unexplained phenomenon. Following this phase in relative hardness is the PP flare spectrum. The PP hardness is explained by the increase in N_H seen in our data (see below) and previously (Haberl 1991). The other softest spectral phases include apastron.

Below we describe the following aspects of the *ASCA* and *RXTE* spectra: the 5-50 keV continuum spectra, the 6-7 keV iron emission and absorption, and possible cyclotron line features. Analysis of the spectrum below 5 keV for which a soft excess including emission features has been reported (e.g. Saraswat et al. 1996) is left for elsewhere??? There is no significant variability in the spectra with pulse phase. Table 2 shows the continuum and iron parameters for the six observations, while Table 3 lists the high-energy parameters. A word here about the errors listed in the tables. These are "1-σ" errors determined by small deviations of the parameters around their best fit values. However, for two reasons they do not correspond to a strict statistical definition of 1-σ. Most importantly the fits are not acceptable, having reduced χ^2, χ^2_R = 1.5-2.5, and thus statistical limits on the parameters lose their meaning. Second, the models are so complex that there exist other minima in the multi-dimensional χ^2 that approach the same values. Nevertheless the models do follow the data at the ~1 percent level and allow for comparisons with past and future results.

3.2.1 5-50 keV Continua

The average spectra at different orbital phases are power laws with low energy absorption and high energy exponential cutoffs. This is typical of many X-ray pulsar spectra (e.g White, Swank, & Holt 1983). For the *ASCA* spectra, 5-10 keV, we present the joint fit of the four detectors??? For *RXTE* spectra, 5-100 keV, we combine the data and response matrices from six PCA detectors and fit models simultaneously with the data contemporaneously obtained with the two HEXTE detectors, the latter analyzed separately from each other. Because exact dead-time corrections are not available for the HEXTE data in the "bin" mode we allowed the HEXTE normalization to float relative to the PCA. Since there was substantial overlap in these data, 20-50 keV, this procedure results in a good estimate of the relative normalization, which was in the range 0.24-0.33, consistent with expectations.

The best-fit photon index ranges over 0.6-1.4. The low-energy absorption model uses Balucinska-Church and McCammon (refs???) cross-sections with all the elemental abundances set to their solar values except for iron which is set to zero. Iron absorption is accounted for separately in an edge component as described below. The low energy absorption is highest during the PP spectra (*AP* and *XP*), consistent with the secondary peak in Figure 7. The only spectra in the phase region of the primary peak of Figure 7 is the *AQ* spectrum. It also exhibits higher low-energy absorption.

The high energy cutoffs and e-folding energies are shown in Table 3. The former range from 20-24 keV and the latter from 6-10 keV, similar to prior results (e.g. Borkus et al. 1998).

3.3.2 Iron Features

We observe the ~6.4 keV line as reported by other observers (e.g. Leahy et al. 1989, P95) in both the *ASCA* and PCA data. This line is identified with neutral Fe Kα. The equivalent widths (e.w.) are in the range from 100-800 eV. In the *ASCA* data there is also evidence for Kβ emission at 7.06 keV. An iron edge near 7.3 keV is also evident in all the data. Table 2 shows the e.w., line photon intensities, line energies, edge energies and edge depths for all the spectra.

3.3.3 >10 KeV Features Observed with RXTE

For all three *RXTE* spectra the PCA data near 10 keV and the PCA and HEXTE data near 20 keV show significant but small (<5%) deviations from the simple continuum model, power law with high energy cutoffs, described above. To further confirm the non-instrumental reality of this feature, we compared the XP data to Crab data from the *RXTE* archive taken near the time (TJD=10383) of the XP observations. The Crab is an example of a featureless powerlaw over most of its *RXTE* range (but see Pravdo, Angelini, & Harding 1997 for a detailed discussion of the *RXTE* Crab spectra). Figure 8a shows the ratio of the GX301-2/Crab counts normalized to the total counts in the channels from 8-16 keV. Any features in the detector response should be eliminated by this procedure, assuming small detector gain drifts between the two observations. The ratio of two featureless powerlaws would be another featureless powerlaw. Instead we see the depression in the GX301-2 spectrum near 10 keV at the couple % level (Figure 8b).

Including a cyclotron absorption component of the form suggested by Makishima et al. (1990), improves the fit considerably. In the XP spectrum, for example, χ^2_R drops from 13.3 to 1.5. Figure 9 shows the XP spectrum, PCA and HEXTE data, plotted versus the best-fit model with (below) and without (above) the cyclotron absorption component added. The energy, depth, and width of the fundamental and first harmonic cyclotron absorption features are shown in Table 3.

4. DISCUSSION

4.1 PULSE PERIOD

The pulse periods measured herein with *ASCA/RXTE* are consistent with the trend seen by the monitoring observations of BATSE. It is interesting to note, however, the exact period

determinations differ, we believe, because of the much shorter measurement time spans in the former compared with the latter. The higher *ASCA/RXTE* source counting rates allow accurate period determinations in shorter time spans. The apparent discrepancies are exacerbated during the periastron phase observations, AP and XP, as shown in Table 1. This may be an indication that the mass transfer during this phase, is not only larger but also more turbulent leading to increased noise in the period behavior, and larger shorter term period excursions. The pulse shape variability (Figure 2) also supports the idea of turbulence.

The long-term period history (Figure 3) shows what may be a fundamental change in the GX301-2 spin behavior. The epoch starting around JD 2448000, which includes the period data reported herein, more resembles the stochastic period behavior in the pre-JD 2446000 epoch. Or, it might be the beginning of a long-term spin behavior reversal such as has been observed in GX 1+4 and 4U1626-67 (Bildsten et al. 1997).

The origins of spin period behavioral changes in accreting pulsars are not well understood. For GX301-2 we see evidence for an accompanying increase in the accretion rate as evidenced by the increased X-ray luminosity (Figure 4). Furthermore, this increase is attributed to the constant component of the X-rays rather than either of the flares. Could this mean an increase in the stellar wind, something that would contribute to an intensity increase at all orbital phases? It would also shift the balance in the period behavior toward stochastic changes, interrupting the steady spin-up associated with an accretion disk.

Jetzer, Strässle, & Straumann (1998) discuss a model in which a small precession of the pulsar inclination angle between its magnetic and rotation axis can lead to spin up and down reversals. Whether this would be triggered by or accompanied by an accretion change, however, in discussed.

4.2 THE ORBITAL LIGHT CURVE

The orbital light curve has epochal changes (see §3.1.2), but it is not clear whether this can be correlated with epochal changes in the pulse period behavior. Two phenomena are suggested by our empirical fits to the orbital light curve. First, the NA flare, present at an earlier epoch, is now undetectable. Second, there is an overall rise in the source intensity that can be accounted for by a rise in the non-flaring, steady component. The latter phenomenon suggests that a largely phase-independent component, such as a canonical, spherically symmetric stellar wind, may now be making a higher relative contribution to the total X-ray emission. Inn addition, the decline in the NA flare's strength may be indicative of a reduction of the phase-dependent component, perhaps because the circumstellar disk is now smaller, so that the NA passage accretes less material. Below, we discuss a model for the phase-dependent component, wherein material from an equatorially-enhanced circumstellar disk around WRA 977 is accreted into a disk around the neutron star GX301-2.

In our model, the timing, strength, and shape of both the PP and the NA flare are explained by the viscous time delay of the matter in the putative GX 301-2 accretion disk in reaching the neutron star. It is clear that an accretion disk should exist during the epochs of steady spinup (see Ghosh & Lamb 1979), and quite possibly beyond these epochs. As suggested in P95, we envisage *two* passages of the neutron star per orbital period through a circumstellar disk around WRA 977 whose plane is tilted with respect to the orbital plane of GX 301-2, and therefore two flares. An exception would occur when the radial extent of the tilted disk is so small that it presents negligible

material to the neutron star during its NA passage (which occurs further away from the companion than its PP passage): in this case we expect only one (PP) flare per orbit. Plausibility of the existence of such tilted disks around massive companions in X-ray binaries, and in their progenitors, massive radio-pulsar binaries like PSR B1259-63, has been increasingly argued in recent years (see Ghosh 1995 and the refences therein). The underlying argument is that the orientation of the orbital plane is correlated with the velocity kick received by the neutron star at birth, and so with the systemic velocity, neither of which is related to the orientations of the rotation axis of the massive companion that determines the plane of its (equatorial) circumstellar disk. Whereas tidal torques would tend to circularize the orbit as well as to coalign the above two planes, it is obvious that a very eccentric system like GX 301-2 is also very likely to retain much of the original tilt between the planes of the circumstellar disk and the orbit. During each of its passages through the disk around WRA 977, a ring of accreting matter is deposited around the neutron star at a radius r_{out} determined by the angular momentum content l_{acc} of the accreted matter. l_{acc} is determined, in turn, by the orbital dynamics, and that of the slow, wind-like outward flow of matter (Waters 1986; Bjorkman & Cassinelli 1993) in the circumstellar disk. Viscous forces spread the ring into an accretion disk on the viscous timescale, t_{visc}, characteristic of the radius r_{out} (Lynden-Bell & Pringle 1974, hereafter LBP; Lightman 1974, hereafter L74), so that most of the ring's mass reaches the neutron star with a time-lag and a spread both of order t_{visc}, producing the X-ray flare. The pre-periastron passage through the circumstellar disk (see below) produces the PP flare, and the other passage (when present), the NA flare. Finally, we think it is plausible that a given passage through the circumstellar disk will tend to truncate the last remnants of the well-developed accretion disk from the previous passage, due to the tidal and thermal forces of the matter in the dense circumstellar disk as the neutron star first plunges into it anew. However, this last point is a minor one: if small vestiges of previous accretion disks persist, they can only cause small deviations from a precise periodicity of the X-ray light curve at the orbital period.

For modeling the orbital lightcurve of GX 301-2, the model parameters of essential importance are (a) the position of the (nodal) line of intersection between the planes of the circumstellar disk and the orbit, as measured by the angular position, ω, of the pre-periastron passage through the disk, (b) the thickness of the circumstellar disk at the point of passage, and (c) the viscous timescale t_{visc} of the accretion disk acquired during the passage. To a smaller extent, the scale and profile of the matter density in the circumstellar disk are also involved. We show below that, if we adopt a specific prescription for t_{visc}, the ratio of the values of this timescale during the two passages through the circumstellar disk is determined entirely by the orbital geometry through the angle ω,, which is thus the most important parameter. Such connection between the properties of the PP and NA flares is, of course, a characteristic feature of all models of this class, and so can serve as a major diagnostic of their viability. The generic lightcurve is given by:

$$L = a\,F_1\left(\frac{\phi-\phi_1}{\Delta\phi_1}\right) + F_2\left(\frac{\phi-\phi_2}{\Delta\phi_2}\right), \qquad (1)$$

where $\phi \equiv t/P_{orb}$ is the orbital phase, ϕ_1 and ϕ_2 are the phases of the first ($\equiv$ PP) and second ($\equiv$ NA) passages through the cir umstellar disk, and the viscous timescales of the accretion disks created in these passages are given by $\Delta\phi_i \equiv t_{visc}^{(i)}/P_{orb}$. The profiles F_i (i = 1,2) represent the viscous evolutions of accretion disks acquired during the i^{th} passage through the thick circumstellar disk, taking into account the disk's thickness (see below). F_i are proportional to the accretion rates through the inner edge of the disk. The relative strengths of the two flares is determined by the parameter a, which depends only on the density profile of the circumstellar disk for given values of ω, and $t_{visc}^{(i)}$. In general, equation (1) can also include a term which is either constant or varies smoothly and moderately at the orbital period, representing accretion through other channels (e.g., a spherically symmetric, low-density wind from WRA 977).

For quantitative modelings reported here, we use analytic approximations to the results of actual theoretical calculations of the viscous evolution of mass rings into accretion disks (LBP, L74). These results are expressed as forms for the viscous evolution profile $F_i(\tau)$, in terms of the dimensionless time, $\tau \equiv \frac{\phi - \phi_i}{\Delta\phi} \equiv \frac{t - t_i}{t_{visc}^{(i)}}$, introduced above ($i$=1,2), the time of the i^{th} passage through the equatorial plane of a *thick* circumstellar disk being measured by t_i or ϕ_i. The calculations of LBP and L74 provide the viscous evolution profile $f(\tau)$ of a mass ring, deposited at $\tau = 0$, into an accretion disk. The analytic treatment of LBP, which neglected the internal thermal structure of the disk, led to a profile of the form $f(\tau) = \tau^{-5/4} \exp\left(-1/\tau\right)$. Evolution of the more realistic disk model of Shakura \& Sunyaev (1973, hereafter SS73) was studied numerically by L74 for a range of parameters. We find that the resultant range of profiles can be well-approximated by analytic forms

$$f(\tau) = \tau^{-n} \exp\left(-n/\tau\right), \tag{2}$$

with $5/2 \leq n \leq 4$. These profiles reach their maxima at $\tau = 1$ decaying subsequently as τ^{-n}. For this work, we have chosen $n = 4$ as being most representative of the disk viscosity parameter (see below) and the "neutron star-like" boundary conditions (L74) of the problem at hand. We take into account the effects of finite thickness of the circumstellar disk (*i.e.* the fact that the mass rings are deposited over a distribution of times) by convolving the above profile f with a suitable distribution g representing the effects of successive disk layers:

$$F_i(\tau) = \int_{-1}^{\min(1, y_h)} f(\tau - \mu^{(i)} y) g(y) dy \tag{3}$$

Here $\mu^{(i)} \equiv t_{disk}^{(i)} / t_{visc}^{(i)}$ where $t_{disk}^{(i)}$ is the semi-thickness of the circumstellar disk at the i^{th} passage measured in units of time (i.e. the time taken by the neutron star to traverse this thickness), and y is a dimensionless co-ordinate normal to the disk's equatorial plane. The upper limit of the integral is constrained to the minimum of 1 or the value $y_h = \left((\phi - \phi) / (t_{disk}^{(i)} / P) \right) - 1$ to account for the fact that the integration is up to the top layer of the disk except when the neutron star is inside the disk. Then the integration stops at the neutron star position. We have explored various disk profiles g and find that their effect is relatively small. Almost identical final results, shown below, hold for either Gaussian or parabolic profiles.

For viscous timescales, we use the standard estimate (L74, LBP)

$$t_{visc} = (2\pi/\alpha)(h/r)^{-2} \sqrt{r_{out}^3 / GM_{ns}}, \tag{4}$$

where α is the usual viscosity parameter of the accretion disk (SS73), h is the semi-thickness of the accretion disk at a radius r from the neutron star, and M_{ns} is the neutron star's mass. As indicated above, the ring radius r_{out} is determined by the specific angular momentum l_{acc} (with respect to the neutron star) of the matter accreted from circumstellar disk by the relation $l_{acc} = \sqrt{GM_{ns} r_{out}}$. As shown by Shapiro & Lightman (1976), this angular momentum is given by $l_{acc} \cong \frac{1}{2} v_{orb} \left(r_a^2 / R \right)$ where v_{orb} is the orbital velocity of the neutron star, R is the distance between the two stars (a function of orbital phase in an eccentric binary like GX 301-2), and $r_a \equiv \xi GM_{ns} / v_{rel}^2$ is the accretion radius. Here, $v_{rel}^2 \approx v_{orb}^2 + v_{wind}^2$ is the relative velocity between the matter in the slow, dense wind of the circumstellar disk and the neutron star, and $\xi \sim 1$ is a dimensionless parameter. In GX 301-2, v_{rel} is dominated by the orbital velocity term. With the aid of these estimates and equation (2), together with standard expressions for the geometry and dynamics of eccentric orbits, we finally obtain

$$\frac{t_{visc}}{P_{orb}} \cong 0.78 \xi^6 \frac{(1-\varepsilon^2)^{3/2}}{(1+\varepsilon\cos\theta)^6} \left(\frac{M_{tot}/M_{ns}}{20} \right)^{-4}. \tag{5}$$

Here, ε is the orbital eccentricity, θ is the true anomaly, i.e., the actual angular position of the neutron star in the orbit with respect to the periastron, M_{tot} is the total mass of the binary, and we have set the

accretion disk parameters to their canonical values $\alpha \cong 1$ and $h/r \cong 0.01$ (SS73). Upon substitution of the known orbital period, eccentricity, and estimate of the massive companion's mass (~$30M_{\odot}$, see Parkes et.al. 1980) for GX 301-2, this yields

$$t_{visc} \cong 14 \frac{\xi^6}{(1+0.472\cos\theta)^6} \text{ day.} \quad (6)$$

Figure 10a shows a fit to the GX 301-2 lightcurve, during the P95 epoch when the NA flare was prominent. This fit is about 3 times worse than the empirical fits discussed above. The model does not match well the shape of the PP flare. Nevertheless it reproduces the qualitative features of the PP and NA flares. We find that $\omega \sim 66$ deg is the best-fit value for a model with the NA flare, with the entire range of acceptable values of ω within a few degrees of this, due to the extreme sensitivity to this parameter. This comes from the sensitive dependence of the viscous timescale on the orbital phase, which is evident from equations (5) and (6). The fitted values of the viscous timescales at the first and second passages through the circumstellar disk are 1.6 days and 8.3 days. The width in days for the PP passage is 2.8. For setting the scale of the constant a in equation (1) (see discussion above), we have chosen a canonical power-law density profile with an exponent ~3 in the circumstellar disk (Waters 1986, Bjorkman & Cassinelli 1993).

The neutral column density (N_H) also changes with orbital phase as a consequence of the material in the circumstellar disk. Figure 10b shows the model predictions for N_H using the same disk parameters as above. The high N_H observed during PP flares, XP and AP, is expected in this model. High N_H observed at other phases (e.g. XA, AQ) may be the result of the interaction between the soft X-ray excess and the higher energy spectrum in the modeling. An observation with higher spectral resolution than *RXTE* and higher sensitivity than *ASCA* below <5 keV, may be successful in untangling these spectral components.

4.3 THE PULSE-PHASE-AVERAGED BROADBAND X-RAY SPECTRUM

4.3.1 Spectral consequences of the orbital light curve model

The spectrum as a function of orbital phase depends upon both the X-rays we view directly from the neutron star surface and the X-rays we view scattered and absorbed by the circumstellar material, where "circumstellar" in the broad sense includes all the matter from the vicinity of the neutron star and outward, the circumstellar disk and stellar wind. Variable accretion onto the neutron star changes the intensity of the direct component and could in principle change its spectrum, but we do not consider that possibility herein.

The relative orientation of the neutron star, the circumstellar disk, and the observer, change during the orbit and is expected to have spectral consequences. For one, the amount of neutral material in the line of sight changes significantly depending upon whether the circumstellar disk is between us and the neutron star, and how much of the denser equatorial portion of the disk is traversed by the line of sight. A "soft component" introduces a complication in testing a model with spectral measurements of N_H as a tracer of cold material. That is because N_H is critically dependent

on the spectral slope at E < 5 KeV where the continuum and line contributions from the soft component are important. This may be responsible for the difficulty in reconciling the measurements of N_H with orbital phase and the data shown in Figure 7c. We would expect an increase in N_H at orbital phase 0.2 if N_H obediently tracked the hardness ratio. Instead, N_H is relatively constant from phase 0-0.5 (Haberl 1991). Orbital phase variability of the soft component is our candidate for resolving this discrepancy, since it contaminates the N_H measurements and decouples the hardness ratio from the N_H measurements.

If we look only at the cold material in the line of sight due to the circumstellar disk then Figure 10b shows the expected N_H variation with orbital phase. The observed increase near periastron is expected from the model.

If the orbital phase dependence of the soft component can be accurately measured in an experiment with good phase coverage, and adequate spectral resolution to separate the spectral components, then we might be in a better position to improve our model for the circumstellar material. For example, does the minimum in X-ray intensity after the PP flare result in a relative minimum in the soft component at that phase? This could account for the increase in the hardness ratio at phase 0.2.

4.3.2 Iron Line Features

The *ASCA* SIS data have among the highest spectral resolution of any GX301-2 data yet reported (<3%). These data do not support the suggestion by Leahy et al. (1989) that there is a correlation between line energy and column density, in particular, that line energy decreases as column density increases. Our measures of column density are in the lower range of Leahy's data where the slope of the suggested correlation is largest. Other correlations between line flux or equivalent width and column density (Leahy et al. 1989, Haberl 1991) are not evident (ASCA???) in our six spectra.

Fe Kβ is expected to accompany Kα on purely physical grounds: if Kα is produced by fluorescence (or most any other mechanism), then the emission occurs when a K shell electron hole is filled by a 2-1 atomic transition. In a fraction of the cases, a 3-1 transition, rather than a 2-1 transition would fill the vacancy. This results in a Kβ photon. The branching ratio of Kβ to Kα photons is 0.134. Kβ emission has been detected in solar flare spectra (Tanaka & Zirin 1985) and has been identified by Phillips et al (1994) as arising from fluorescence. The ratio of Kβ to Kα photons measured from GX 301-2 is ???. This is consistent with the theoretical value and further rules out the presence of significant emission from nearby $Ly\alpha_1$ (6.99 keV) and $Ly\alpha_2$ (6.97 keV). These would arise from highly ionized ions that are apparently not present with an emission measure more than ???

4.3.3 Cyclotron Features

There are two characteristics of the GX 301-2 spectra above 10 keV that suggest the effects of superstrong magnetic fields. They are the high energy cutoff on the one hand and the absorption-like features near 10 and 20 keV on the other. Unfortunately there is no unifying theoretical model that can account for both effects. Boldt et al (1976) introduced the idea that the high energy cutoff itself is a result of modified Thomson scattering in a highly magnetized plasma.

However this model predicts that emission from extraordinary mode of propagation would be cut off below the cyclotron energy, E_H, implying that $E_H > 20$ keV. (The emission from the ordinary mode of propagation is not strongly modified below E_H.) If instead we consider the cyclotron absorption model given in Makishima et al (1990) and used to fit other pulsar spectra (e.g. Orlandini et al. 1998), then the cyclotron energy would be near 10 keV. We conclude that the possible presence of the harmonic absorption feature near 20 keV points more toward the lower E_H. The surface magnetic field would then be about 9×10^{11} G. In that case the cutoff above 20 keV must be due to either an unmodeled magnetic field effect, or an intrinsic fall-off in the underlying spectrum, perhaps indicative of its temperature, ~10 keV.

5. CONCLUSIONS

GX301-2 is an X-ray source that continues to change in interesting ways and reveal its secrets. The spin behavior has apparently entered a new phase. Evidence for what may be cyclotron features near 10 and 20 keV is seen. The orbital light curve varies with time and can be modeled by periodic mass transfers from a WRAY 977 circumstellar disk and the time-scale for viscous accretion in the neturon star's accretion disk.

ACKNOWLEDGMENTS

We thank Dr. M. Finger for providing BATSE/*CGRO* period estimates and for useful discussions. This research has made use of data obtained through the High Energy Astrophysics Archive Research Center (HEASARC), provided by the NASA Goddard Space Flight Center.

REFERENCES

Bildsten, L. et al. 1997, ApJ Suppl, 113, 367
Bjorkman, J.E., & Cassinelli, J. P. 1993, Ap. J., 409, 429
Boldt, E. A., Holt, S. S., Rothschild, R. E., & Serlemitsos, P. J., 1976, A Ap, 50, 161
Borkus, V.V. et al. 1998, Astr. Lett, 24, 83
Chichkov, M. A. et al. 1998, Sov Astron Lett, 1995, 21, 435
Finger, M. 1998, private communication
Fishman, G. J. et al. 1989, in Proc. GRO Science Workshop, ed. W. N. Johnson (Greenbelt: NASA/GSFC), 2-39
Ghosh, P. 1995, Ap. J., 453, 411
Ghosh, P. & Lamb, F. K. 1979, Ap J, 234, 296
Haberl, F. 1991, Ap J, 376, 245
Jetzer, P, Strässle, M, & Straumann, N. 1998, New Astr, 3, 619
Koh, D. 1995, private communication
Koh, D. et al. 1997, ApJ, 479, 933
Layton, J. T., Blondin, J. M.,Owen, M. P. , & Stevens, I. R. 1998, NA, 3, 111
Leahy, D. A. 1991, M N R A S, 250, 310
Leahy, D. A. et al. 1989, M N R A S, 237, 269
Leahy, D. A. & Matsuoka, M. 1990, Ap J, 355, 627
Levine, A. M. et al. 1996, ApJ (Letters), 469, L33

Lightman, A. P. 1974, Ap J 194, 429
Lynden-Bell, D. & Pringle, J. E. 1974, MNRAS, 168, 603
Makishima, K. et al. 1990, ApJ (Letters), 365, L59
Nagase, F. 1989, P A S J, 41, 1
Orlandini, M. et al 1998, Ap J, (Letters), 500, L163
Parkes, G. E. et.al. 1980, MNRAS, 191, 547
Pravdo, S. H. et al. 1995, Ap J, 454, 872
Pravdo, S. H., Angelini, L., & Harding, A. K. 1997, ApJ, 491, 808
Prince, T. A. et al. 1994, in The Evolution of X-ray Binaries, S. S. Holt and C. S. Day, eds, AIP Conf. 308, AIP, New York, p. 235
Ricker, G. R. et al. 1973, Ap J, 184, 237
Robinson, R. D. 1990, Ap J Suppl, 74, 891
Saraswat, P. et al. 1996, ApJ, 463, 726
Sato, N. et al. 1986, Ap J, 304, 241
Shakura, N. I. & Sunyaev, R. A. 1973, A Ap, 24, 337.
Shapiro, S. L. & Lightman, A. P. 1976, Ap J, 204, 555
Stevens, I. R. 1988, M N R A S, 232, 199
Swank, J. H. et al. 1976, Ap J (Letters), 209, L57
Tanaka, K. & Zirin, H. 1985, Ap J, 229, 1036
Tanaka, Y. et al. 1994, P A S J, 46, L37
Waters, L.B.F.M. 1986, A Ap, 162, 121
White, N. E. et al. 1976, Ap J, 209, L119
White, N. E. & Swank, J. H. 1984, Ap J, 287, 856
White, N. E., Swank, J. H., & Holt, S. S. 1983, ApJ, 270, 711

TABLE 1. Observations Summary

Satellite/ ObsID	TJD Start	GX301 Binary Phase	Intensity (c/s)	Pulse Period (s)	BATSE Difference (s)
ASCA/AQ	9396.542	0.30-0.32	1.00±0.01	675.76±0.05	0.11
ASCA/AA	10108.416	0.46-0.48	3.06±0.01	677.34±0.03	-0.04
ASCA/AP	10129.416	0.99-0.98	6.30±0.02	678.00±0.30	0.34
RXTE/XP	10338.008	0.00-0.02	929±1	679.34±0.10	0.35
RXTE/XA	10399.458	0.48-0.49	338±1	679.14±0.07	-0.14
RXTE/XQ	10409.625	0.72-0.75	648±1	679.50±0.02	0.01

Table 2. Continuum and Iron Feature Parameters

ObsID	Norm	α	N_H (10^{22} cm^{-2})	Fe K α EW (eV)	Fe K α Phot (10^{-4})	Fe K α E(keV)	Fe K β EW (eV)	Fe K β Photons (10^{-4})	Fe K β E (keV)	Fe K Edge Depth	Fe K Edge E(keV)
AP			75	823			264				
XP	0.084±0.017	0.63±0.07	50.0±2.8	521±15	135±4	6.32±0.01				0.83±0.04	7.28±0.02
AA			27	127			32				
XA	0.0324±0.021	0.67±0.22	41.6±4.2	838±80	77.8±7.4	6.38±0.02				0.77±0.61	7.38±0.23
AQ			51	212			51				
XQ	0.194±0.012	1.38±0.02	13.8±0.9	99±9	15.1±1.4	6.36±0.12				0.20±0.01	7.36±0.08

Table 3. High Energy/Cyclotron Parameters

ObsID	E_{Cutoff}	$E_{Folding}$	$Depth_0$	$E_{Cyclotron}$	W_0	D_1	W_1
XP	20.6±0.2	6.4±0.2	0.043±0.009	10.1±0.1	1.0±0.7	0.31±0.02	2.9±0.3
XA	20.6±0.5	6.5±0.4	0.19±0.03	10.0±0.2	2.2±0.3	0.29±0.04	2.8±0.5
XQ	23.6±0.2	9.6±0.3	0.025±0.004	10.9±0.1	1.0±1.0	0.15±0.01	2.8±0.7

FIGURE CAPTIONS

1. Phase lags for XP data intervals folded over trial pulse periods.

2. Pulse shapes for XP data intervals folded over the best-fit period.

3. Long term pulse period history

4. Light curve with 20-50 KeV BATSE data. Each point is data averaged over 124.5 days (three orbital periods).

5. Intensity data folded over the 41.5-d orbital period: (a) TJD 8500-xxxx, (b) TJD xxxx-yyyy, (c) TJD yyyy-9500, (d) TJD 9500-10554.

6. Intensity components of the orbital light curve in the four time intervals listed in the preceding figure.

7. (a). ASM intensity data folded over the orbital period from TJD 10087-10554, (b) BATSE intensity data folded over the orbital period from TJD 10087-10554, (c) the ratio of data (b) to data (a).

8. (a) The ratio (points) of the GX301-2 XP count to the Crab counts in the energy channels between 8 and 16 keV. The line through the points is the linear regression to these data. (b) The differences between the ratio and the linear regression in (a).

9. Spectrum taken with *RXTE* during the periastron passage phase. Above is a fit without a cyclotron absorption component. Below includes the cyclotron absorption component.

10. (a) Model of the X-ray light curve based on the existence of a circumstellar disk. Note how variations in the parameters listed in the text change the appearance of the NA flare. (b). Variations in N_H for the same disk parameters as (a).

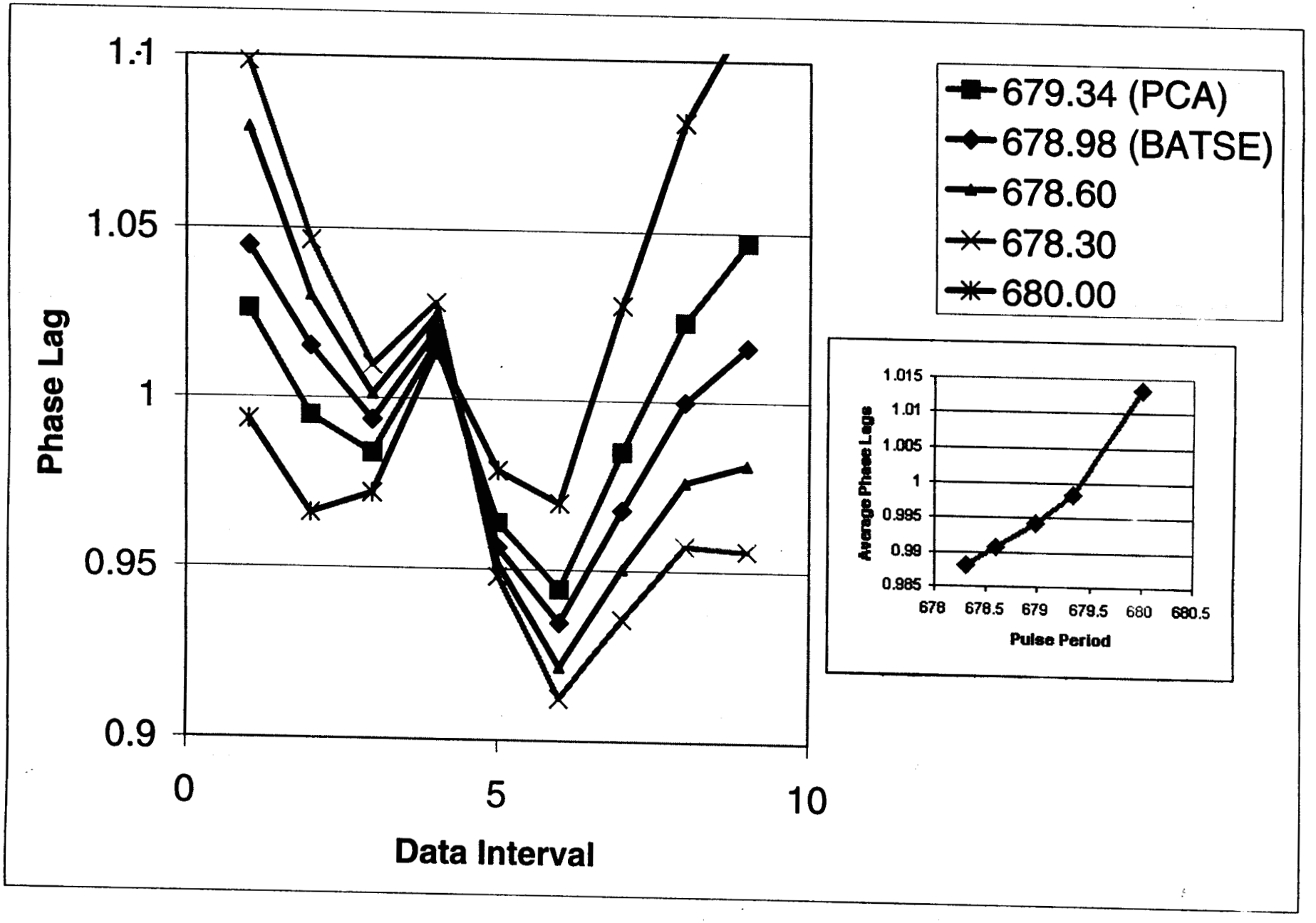
1.1
1.05
1
0.95
0.9
Phase Lag
0
5
10
Data Interval
679.34 (PCA)
678.98 (BATSE)
678.60
678.30
680.00
1.015
1.01
1.005
1
0.995
0.99
0.985
Average Phase Lags
678
678.5
679
679.5
680
680.5
Pulse Period

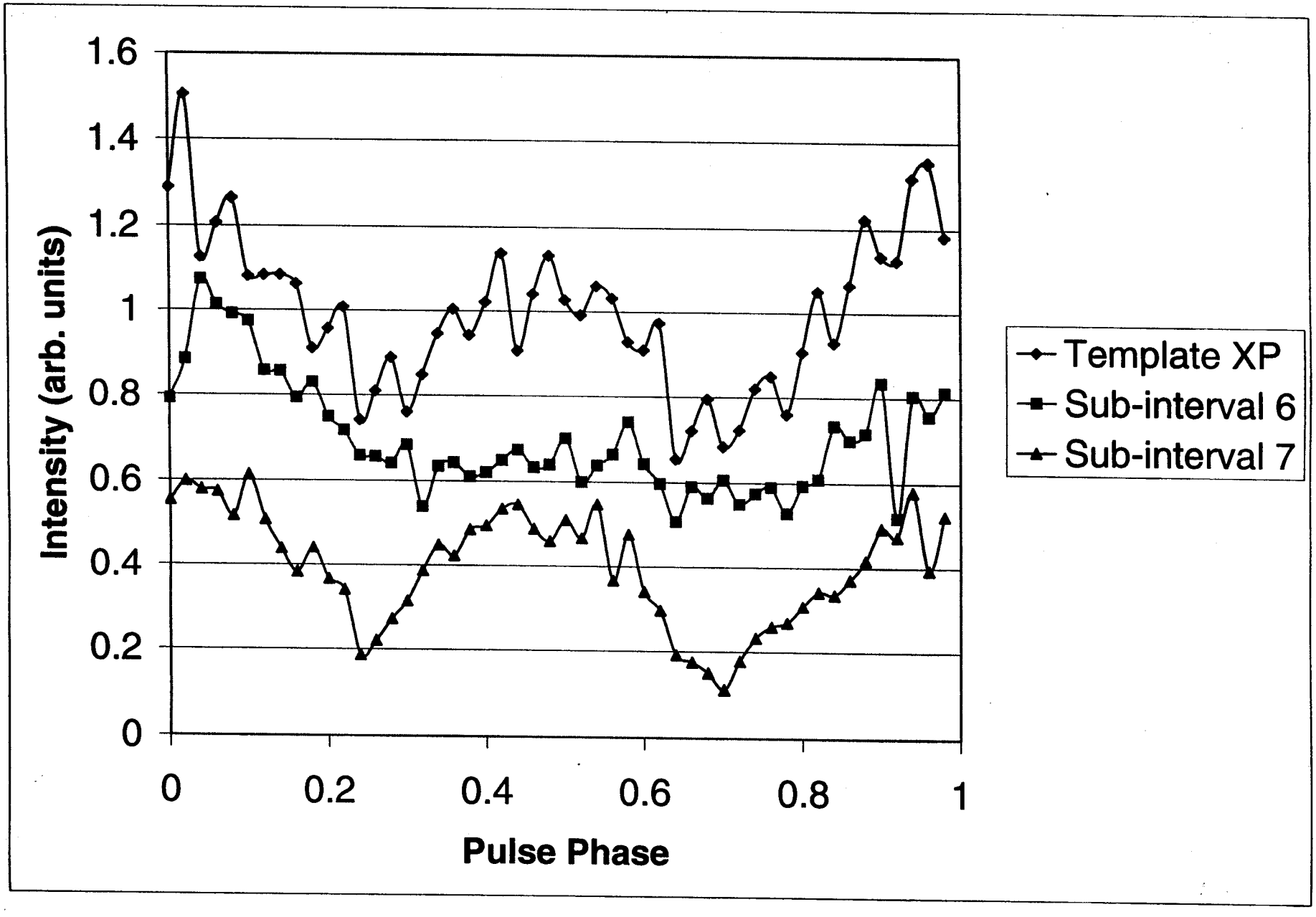
1.6
1.4
1.2
1
0.8
0.6
0.4
0.2
0
Intensity (arb. units)
0
0.2
0.4
0.6
0.8
1
Pulse Phase
Template XP
Sub-interval 6
Sub-interval 7

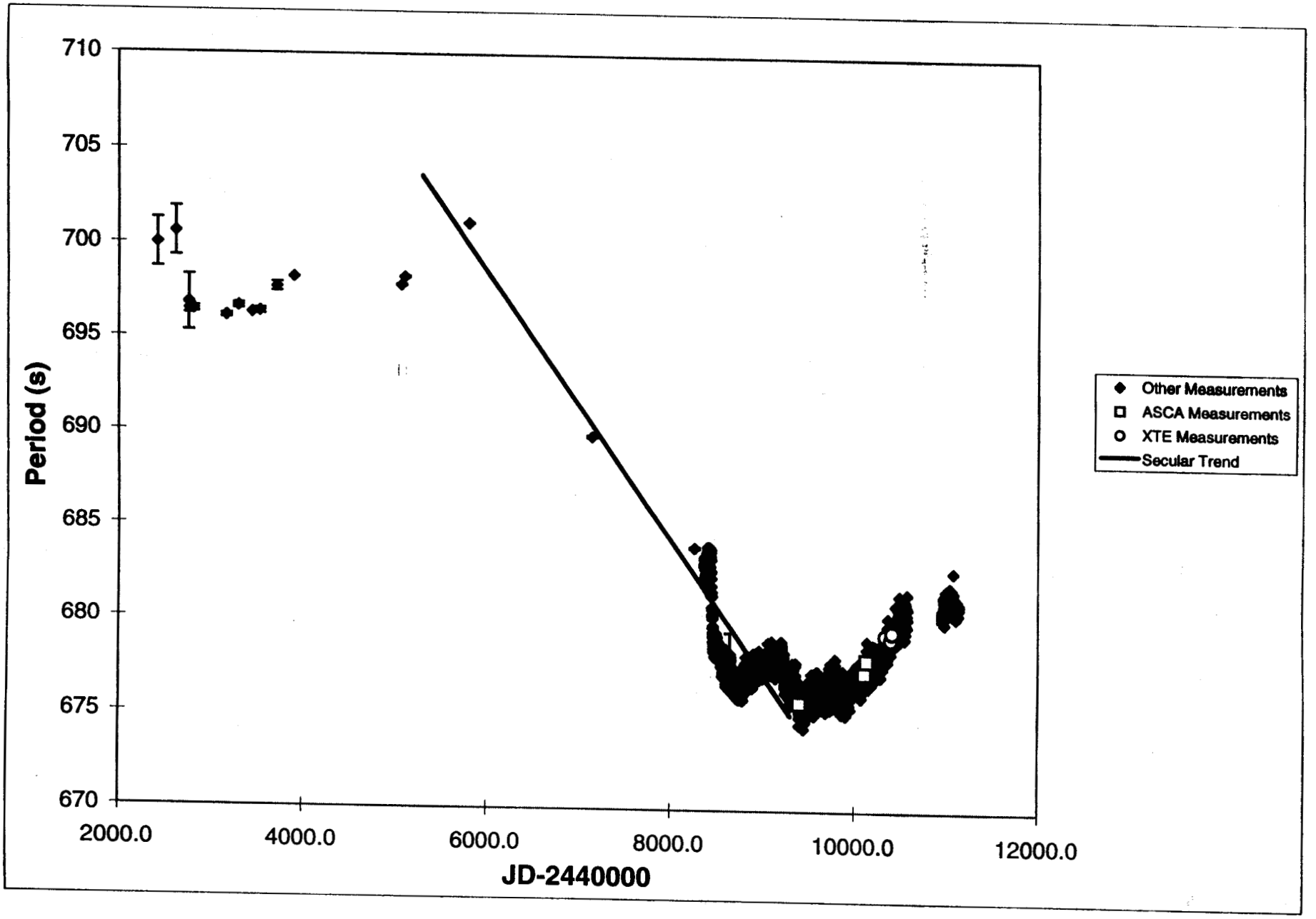
710
705
700
695
690
685
680
675
670
Period (s)
2000.0
4000.0
6000.0
8000.0
10000.0
12000.0
JD-2440000
Other Measurements
ASCA Measurements
XTE Measurements
Secular Trend

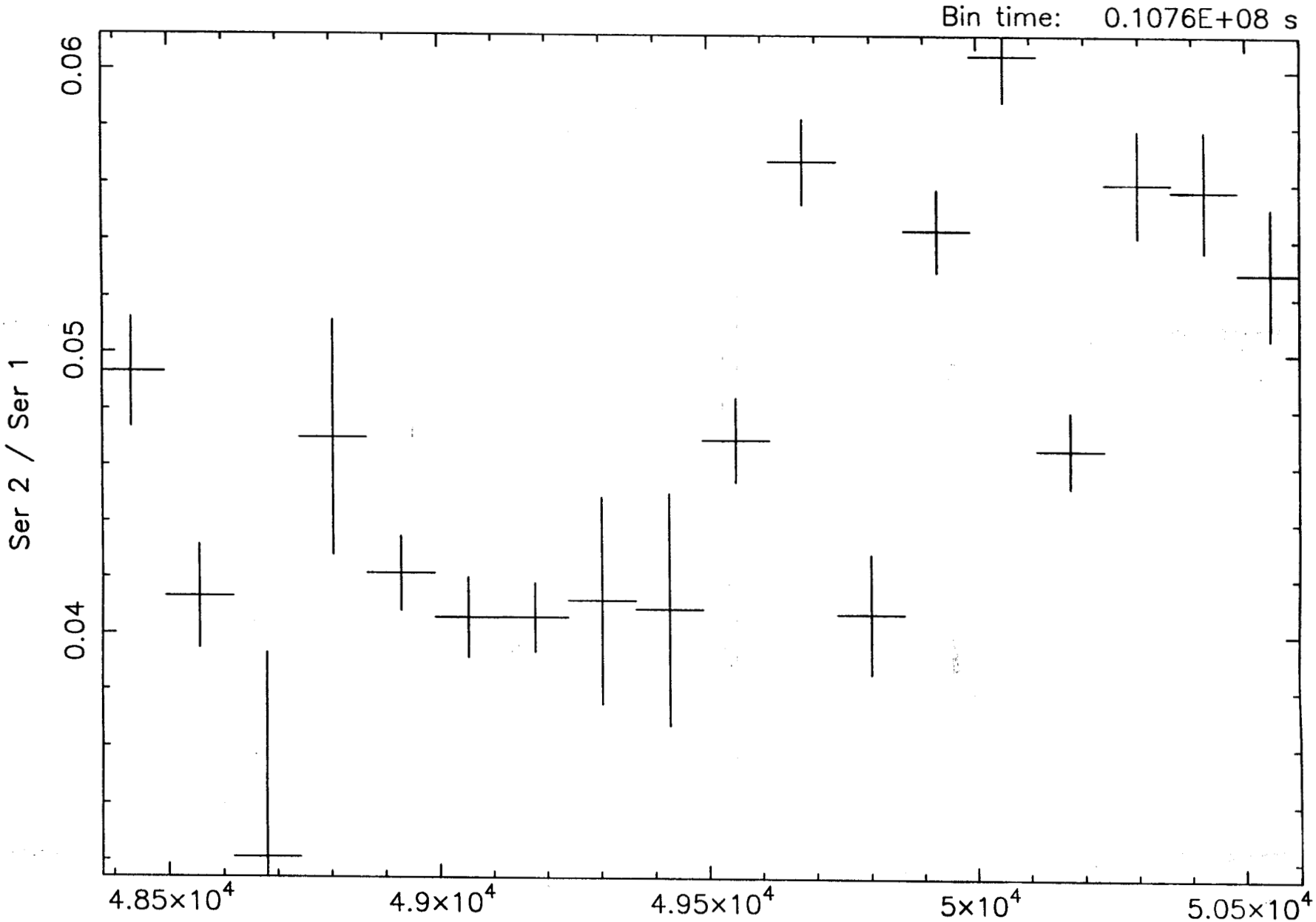

Start Time 48431 17:55:40:800 Stop Time 50548 3:28:48: 0

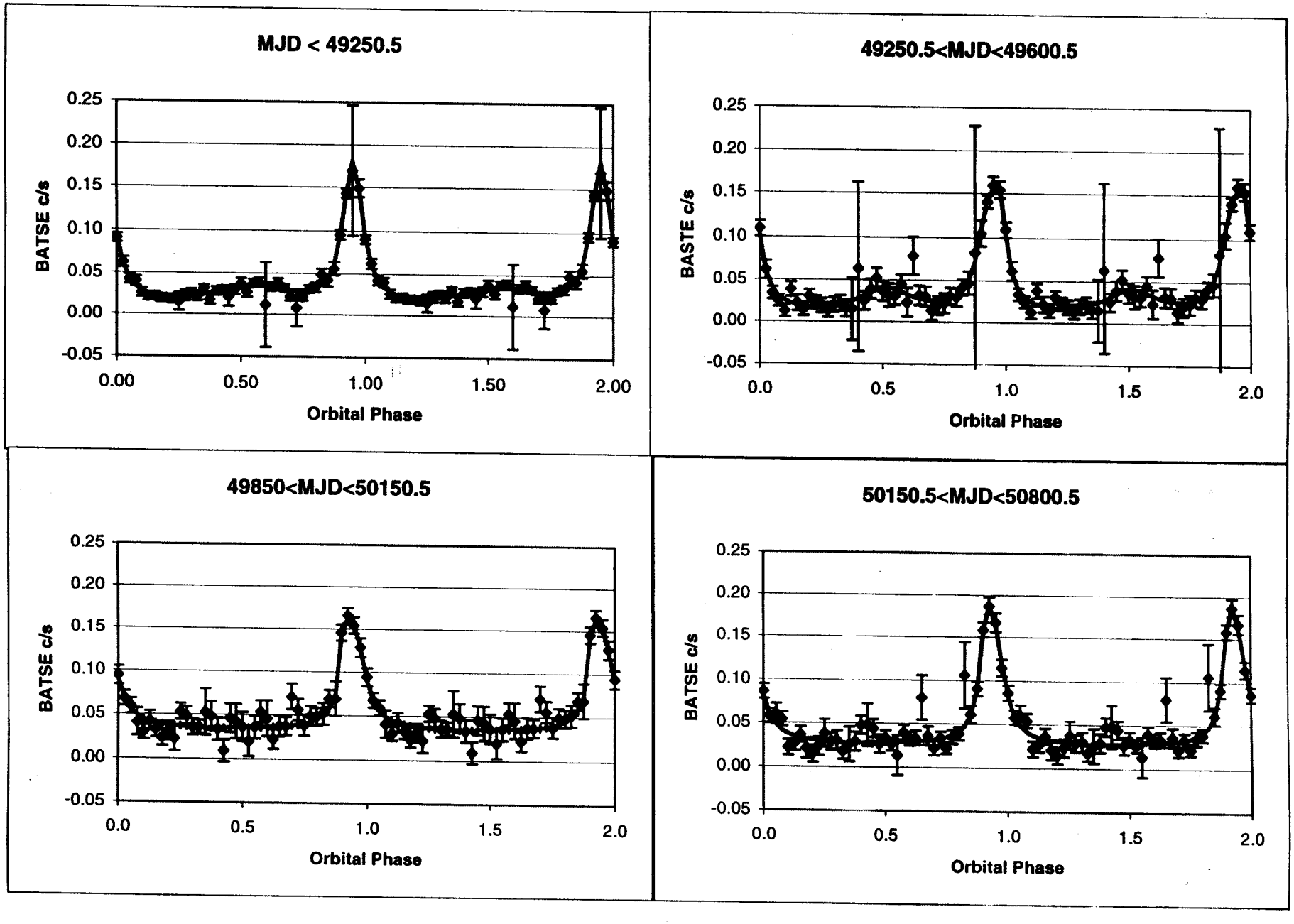
MJD < 49250.5
BATSE c/s
0.25
0.20
0.15
0.10
0.05
0.00
-0.05
0.00
0.50
1.00
1.50
2.00
Orbital Phase
49250.5<MJD<49600.5
BASTE c/s
0.25
0.20
0.15
0.10
0.05
0.00
-0.05
0.0
0.5
1.0
1.5
2.0
Orbital Phase
49850<MJD<50150.5
BATSE c/s
0.25
0.20
0.15
0.10
0.05
0.00
-0.05
0.0
0.5
1.0
1.5
2.0
Orbital Phase
50150.5<MJD<50800.5
BATSE c/s
0.25
0.20
0.15
0.10
0.05
0.00
-0.05
0.0
0.5
1.0
1.5
2.0
Orbital Phase

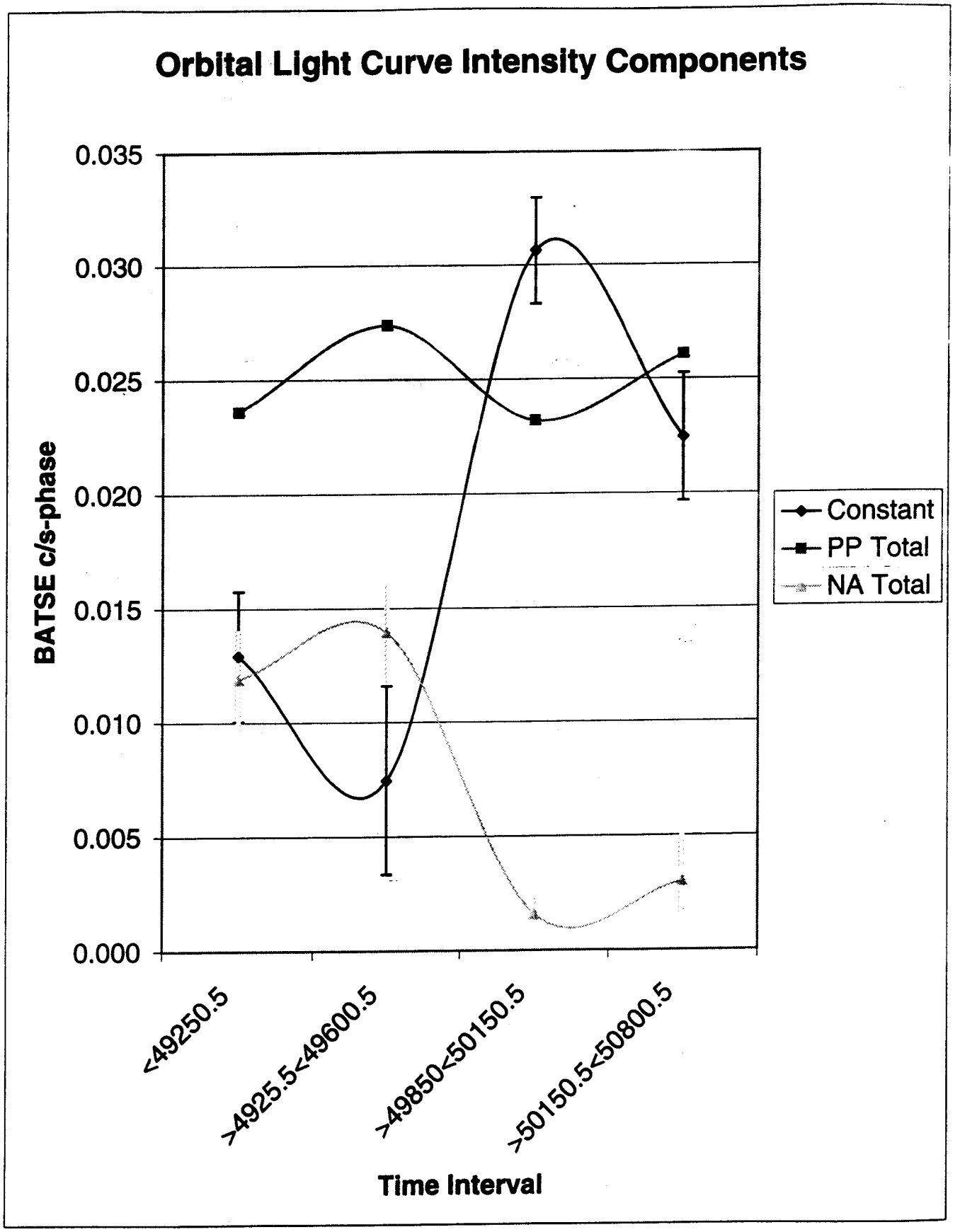
Orbital Light Curve Intensity Components
0.035
0.030
0.025
0.020
0.015
0.010
0.005
0.000
BATSE c/s-phase
Constant
PP Total
NA Total
<49250.5
>4925.5<49600.5
>49850<50150.5
>50150.5<50800.5
Time Interval

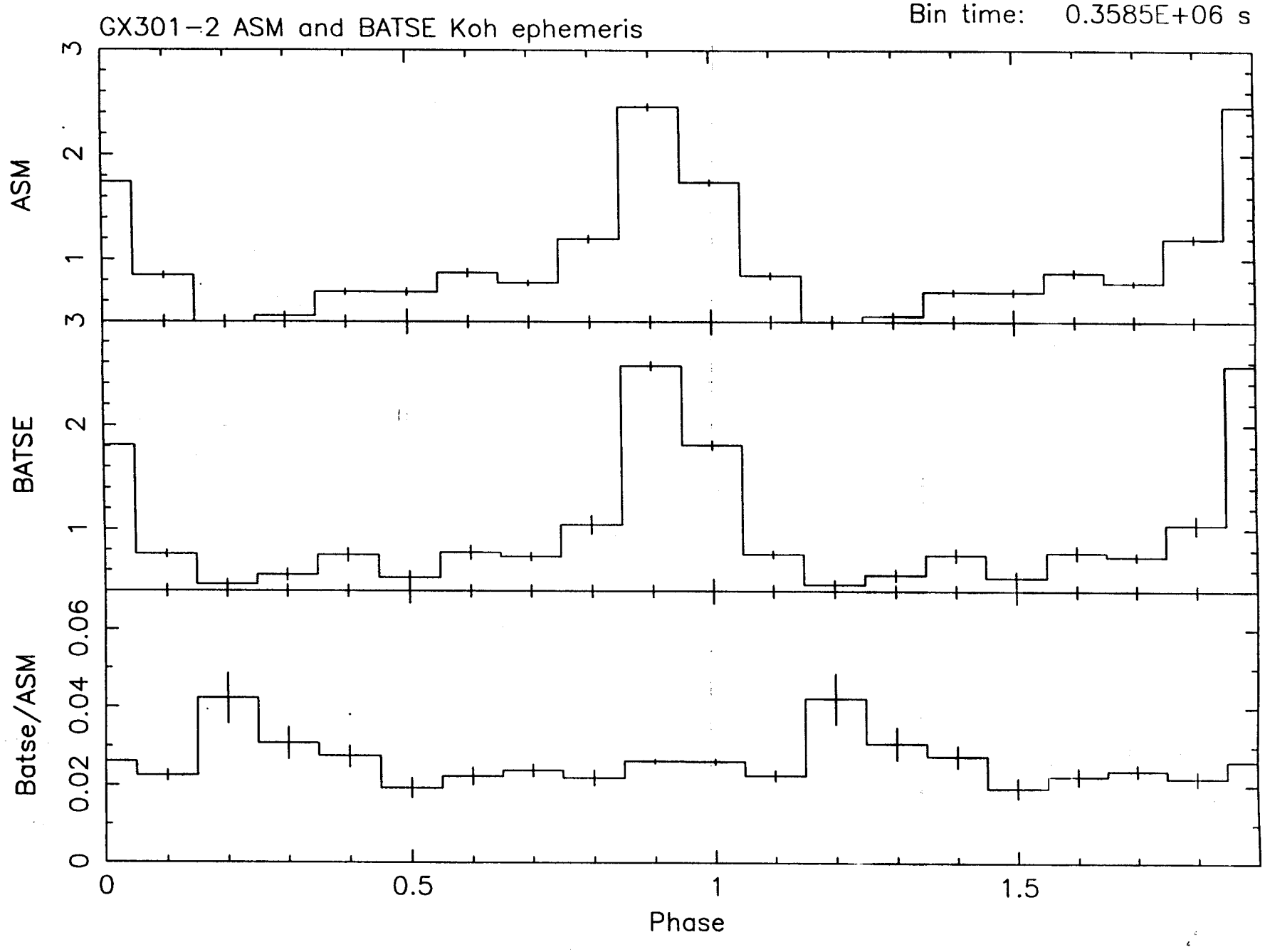

Start Time 50087 13:47:51:360 Stop Time 50554 16:32:29: 40

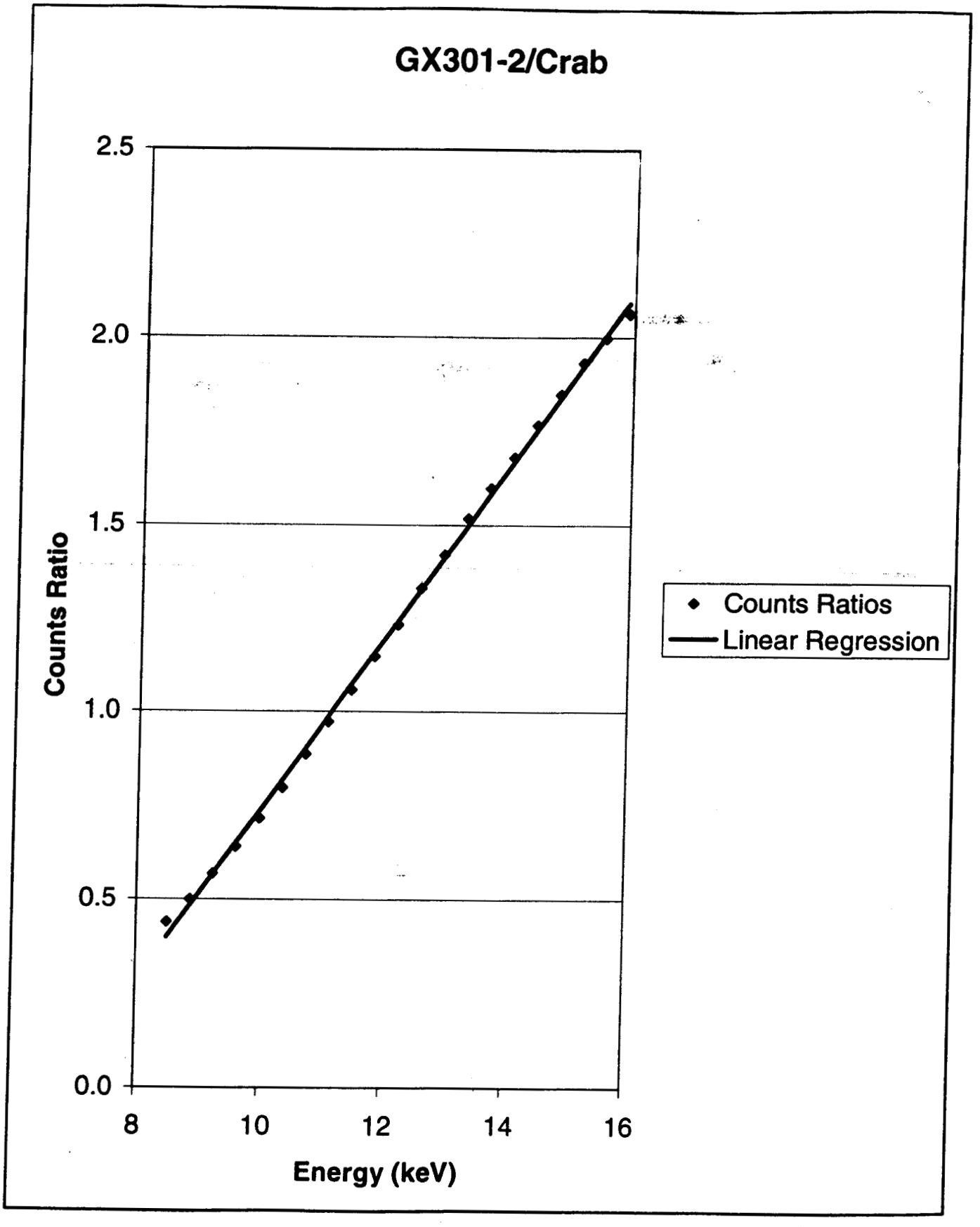
GX301-2/Crab
2.5
2.0
1.5
1.0
0.5
0.0
Counts Ratio
8
10
12
14
16
Energy (keV)
Counts Ratios
Linear Regression

Fig 8

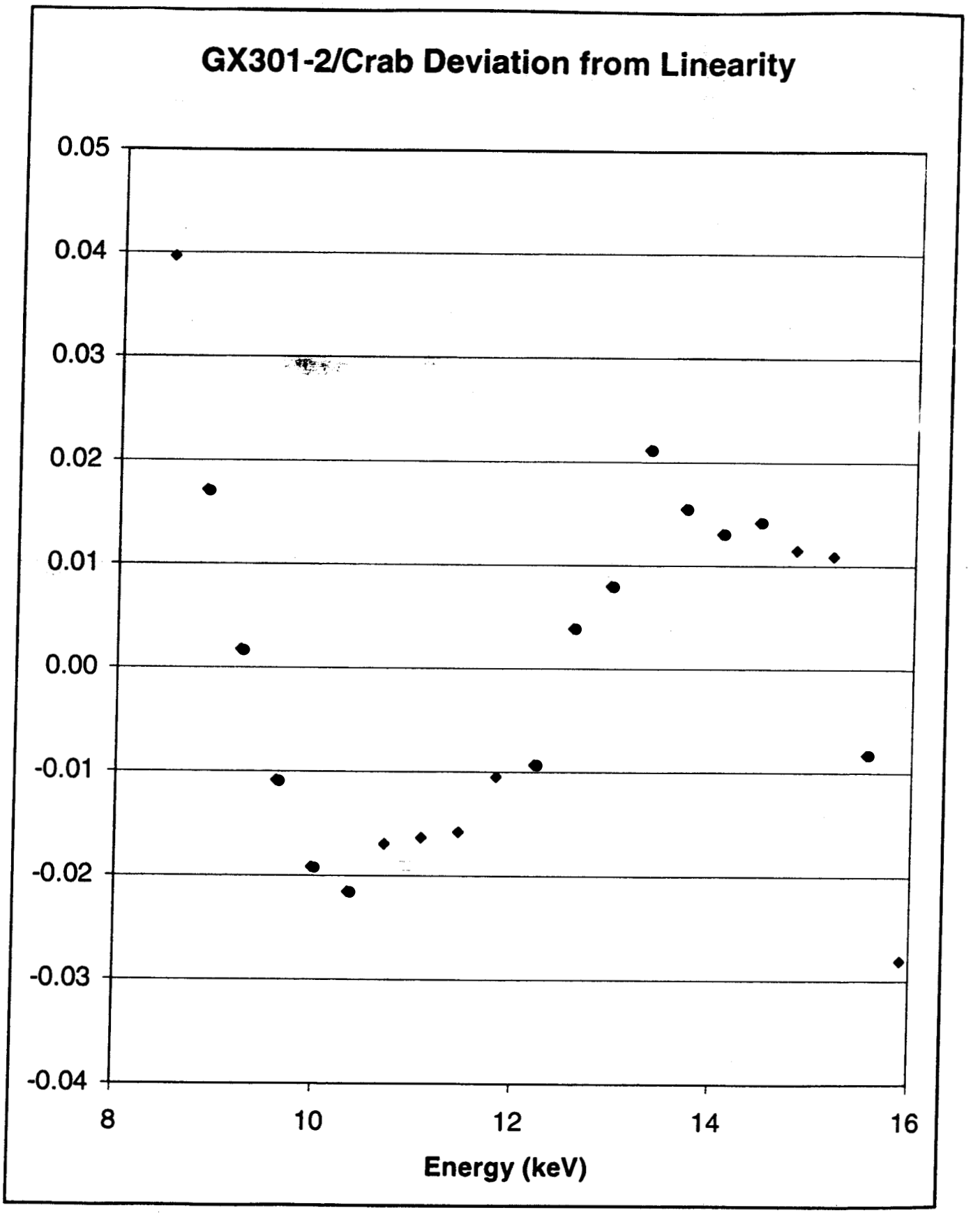
GX301-2/Crab Deviation from Linearity
0.05
0.04
0.03
0.02
0.01
0.00
-0.01
-0.02
-0.03
-0.04
8
10
12
14
16
Energy (keV)

Fig. 8b

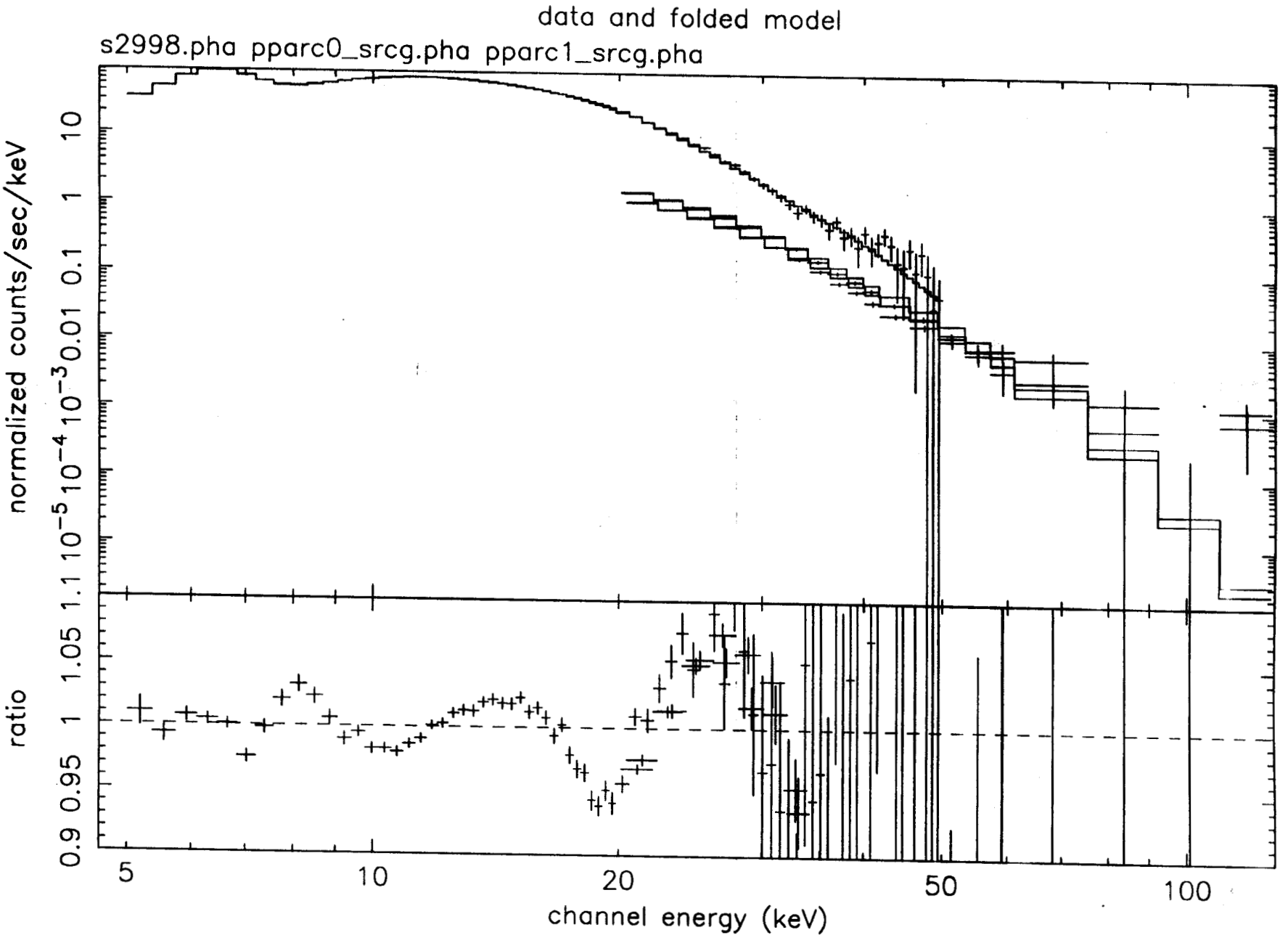

shp 22-Jan-1999 09:44

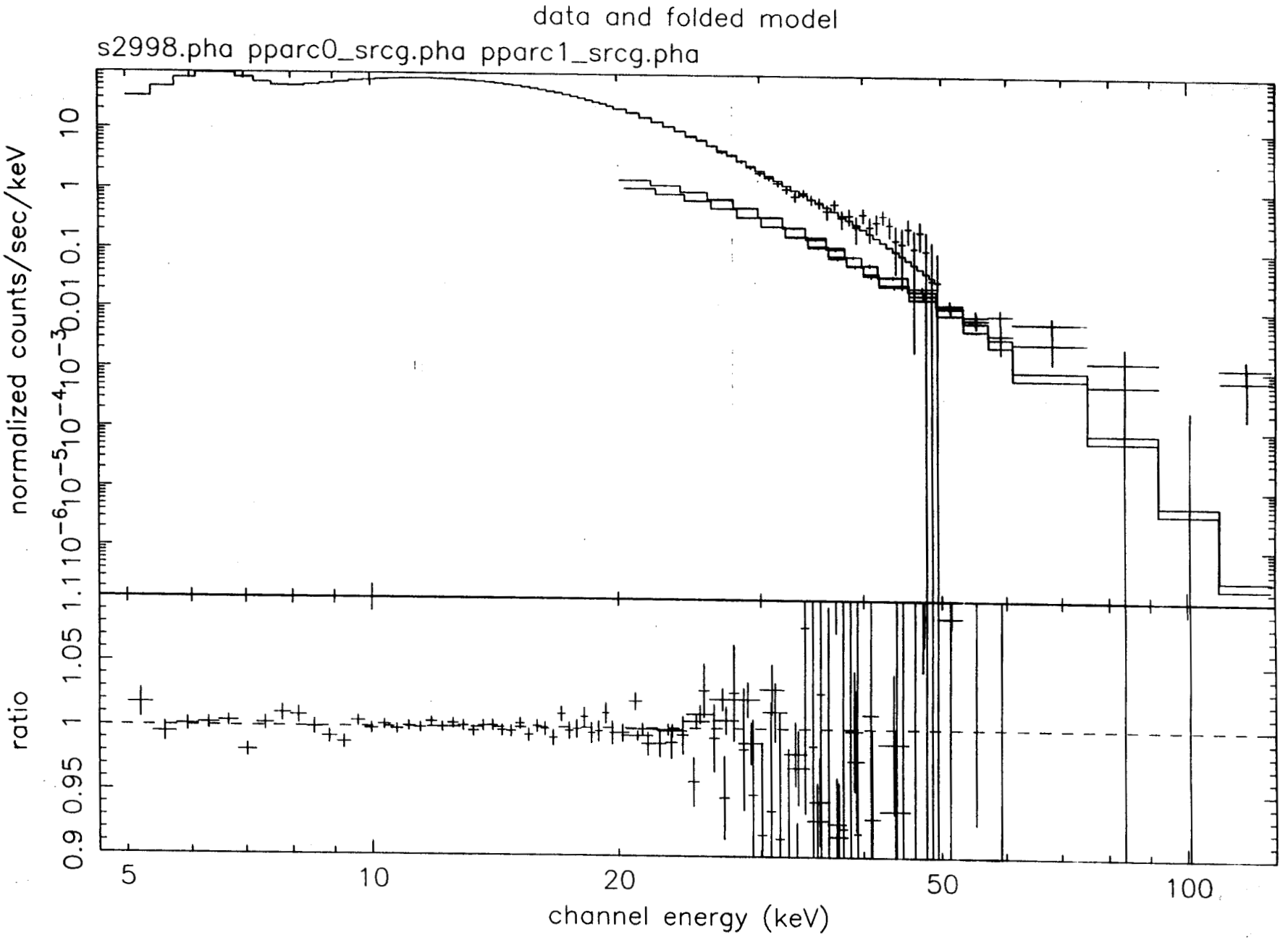

shp 14-Dec-1998 10:34

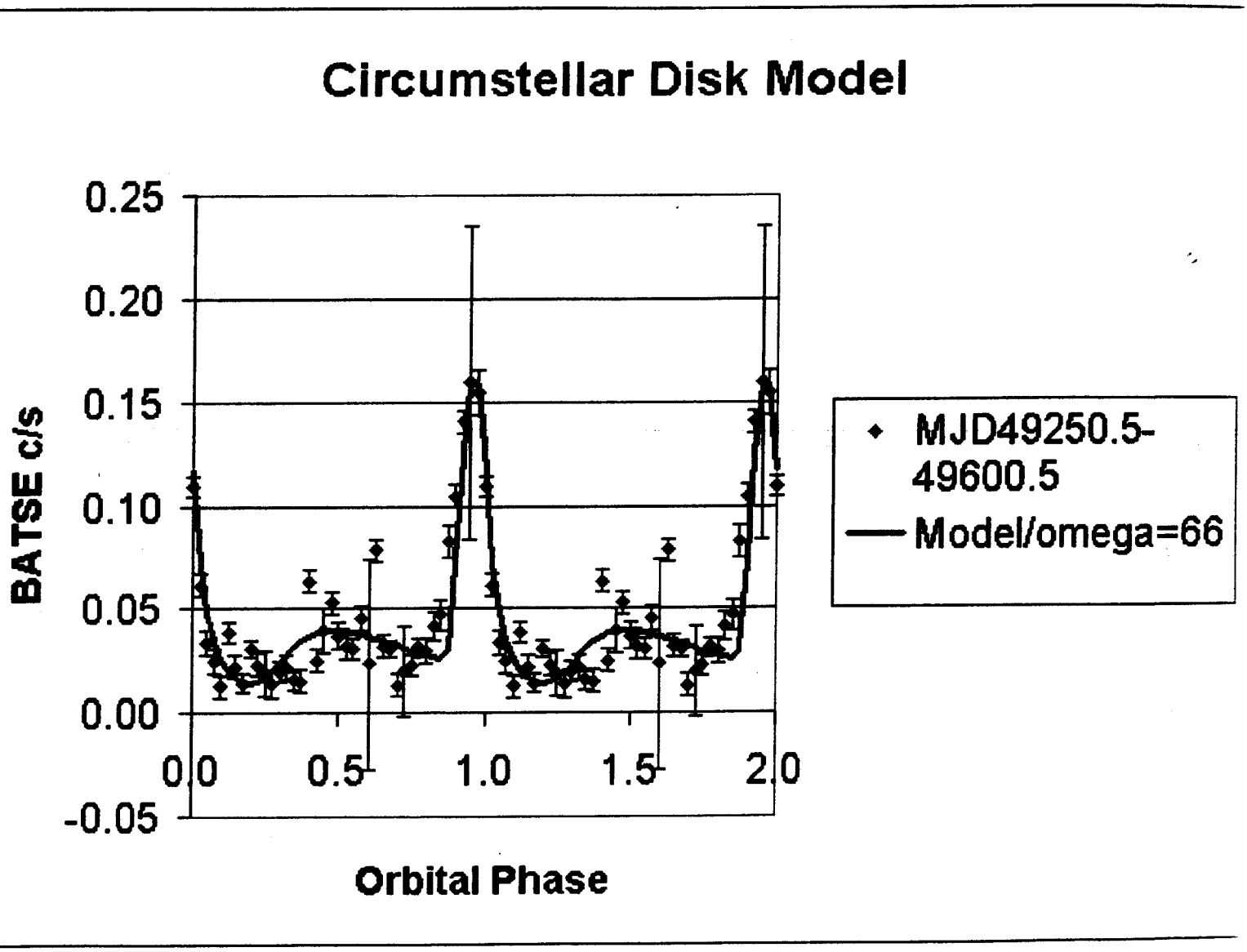
Circumstellar Disk Model
0.25
0.20
0.15
0.10
0.05
0.00
-0.05
BATSE c/s
0.0
0.5
1.0
1.5
2.0
Orbital Phase
MJD49250.5-49600.5
Model/omega=66

10A